A Fast Spectral Method for Active 3D Shape Reconstruction

Jia Li, Alfred O. Hero

Abstract

Variational energy minimization techniques for surface reconstruction are implemented by evolving an active contour according to the solutions of a sequence of elliptic partial differential equations (PDE's). For these techniques, most current approaches to solving the elliptic PDE are iterative involving the implementation of costly finite element methods (FEM) or finite difference methods (FDM). The heavy computational cost of these methods makes practical application to 3D surface reconstruction burdensome. In this paper, we develop a fast spectral method which is applied to 3D active contour reconstruction of star-shaped surfaces parameterized in polar coordinates. For this parameterization the Euler-Lagrange equation is a Helmholtz-type PDE governing a diffusion on the unit sphere. After linearization, we implement a spectral non-iterative solution of the Helmholtz equation by representing the active surface as a double Fourier series over angles in spherical coordinates. We show how this approach can be extended to include volumetric grey-level penalties. A number of 3D examples and simulation results are presented to illustrate the performance of our fast spectral active contour algorithms.

Keywords

Star-shaped surfaces, active contour surface reconstruction, double Fourier series, spherical harmonics, Helmholtz equation.

I. INTRODUCTION

Partial differential equations (PDE's) have been widely applied to solve many computer vision and image processing problems, such as curvature based contour flow, edge-preserving image smoothing, image registration via deformable models, and image segmentation. The advantages of applying PDE methods to image analysis have been summarized in [6]. In particular, some of these problems, such as shape from shading [16], surface reconstruction [31] and active contours [11], can be formulated in the framework of variational principles and lead to solving Euler-Lagrange equations of elliptic type as the necessary condition for a minimum. The need to solve elliptic equations of the general form

$$\nabla^2 u - \epsilon u = f \tag{1}$$

arises in these problems. This equation arises from minimizing an energy function defined as the sum of a data fidelity term and a surface roughness penalty. These methods are thus known as variational methods and energy minimization methods.

This paper is concerned with implementation of fast variational methods for the reconstruction of smooth star-shaped 3D surfaces. The majority of variational approaches to 3D object reconstruction solve PDE's on a rectangular domain, e.g. the plane $\Omega \in \mathbb{R}^2$. Such a 2D representation is natural as a 3D surface is simply a mapping $\mathbf{x} : \Omega \to \mathbb{R}^3$, i.e. $\mathbf{x}(v, w) = (x_1(v, w), x_2(v, w), x_3(v, w))$, where $(v, w) \in \Omega$. These approaches solve the obtained PDE's by iterative techniques, such as finite element methods (FEM) and finite difference methods (FDM). For example, Cohen used FEM to solve the PDE's in active balloons models [9] and in [33] Xu used FDM to solve the PDE's for gradient vector flow. The advantage of FEM methods is their geometric flexibility, in other words, their ability to perform local mesh refinement. However, FEM/FDM have met with difficulties for practical 3D imaging applications. The large number of voxels in 3D images causes significant growth of computation time which is intolerable in most practical applications.

In this paper, we consider fast methods of surface reconstruction and segmentation of 3D star-shape objects using the active balloon framework introduced by Cohen [9]. The surface functions of such objects and the associated PDE's can be defined over the unit sphere S^2 instead of a 2D rectangular domain, where

J. Li is with the Department of Computer Science and Engineering, Oakland University, Rochester, MI, 48309 USA
A. O. Hero is with the Department of Electrical Engineering and Computer Science, The University of Michigan, Ann Arbor, MI, 48109 USA

$S^2 := \{(x, y, z) : x^2 + y^2 + z^2 = 1\}$ in the cartesian coordinate system or $S^2 := \{(r, \theta, \phi) : r = 1\}$ in the spherical coordinate system. With the assumption that the origin has been aligned up with the object center, any star-shaped 3D surface can be naturally modelled by a single valued radial description function, $f(\theta, \phi) : S^2 \rightarrow \mathbb{R}$ defined on the unit sphere. Orthogonal functions on the unit sphere, such as spherical harmonics and double Fourier series have been widely used to decompose the radial descriptor f so that the statistical information of the corresponding coefficients can be used to guide other image processing tasks, such as deformation analysis [15] and image segmentation [28]. In fact, radial descriptor f can be applied to the wide class of any simply connected (no hole) surface which can be embedded into the unit sphere. For example, Brechbühler proposed to parameterize the surfaces of simply connected 3D objects by defining a continuous, one-to-one mapping from the surface of the original object to the surface of a unit sphere [5]. The parameterization is implemented via a constrained optimization procedure. In [30], Tao proposed to build a statistical shape model of cortical sulci by projecting sulci onto the unit sphere and extracting intersubject variability of the shape of the sulci and of the mean curvature along the sulcal curves.

PDE algorithms on the unit sphere have been widely studied for the numerical simulation of turbulence and phase transition, weather prediction and the study of ocean dynamics. In 1970's, spectral methods and pseudo-spectral methods on the unit sphere emerged as a viable alternative to finite difference and finite element methods [2], [3], [23]. It is well known that spectral methods have unsurpassed accuracy for boundaryless or periodic domain like the unit sphere and a faster rate of convergence than that of FDM and FEM in solving PDE's [14]. To further accelerate run-time without loss in accuracy for solving PDE's on the sphere, Cheong [8] and Yee [34] have recently devised less computationally demanding alternatives to the spherical harmonic basis. These results are the prime motivation for applying fast spectral methods to reduce the computation time for evolving 3D deformable surfaces in active balloon reconstruction for broken edge maps [18], [9].

Fourier snakes using spherical harmonic representations have been proposed for 3D deformable shape models by Staib and Duncan [27] and Székely *etal* [29]. The Mumford-Shah energy functional [22] was introduced by Chan to deal with blurred or broken boundary problem [7]. Similar approaches to include region-based grey-level information in segmentation can also be found in [17] and [32]. The work described in this paper combines and extends these approaches in several novel ways. First, we adopt a different total energy functional from [29] and [22] which accounts for an incomplete edge map by using a 3D Chamfer-like distance function [10] to enforce edge information and an internal energy which combines a surface roughness penalty and a grey-scale region-based penalty similar to that used in [12] and [17]. Second, we adopt the variational approach of [9] to minimization of the energy functional and we show that the Euler-Lagrange equations reduce to a non-linear PDE over the unit sphere describing the energy minimizing surface. Third, temporal evolution of the active surface results directly from linearization of this PDE via successive approximations. This linearization leads to an evolving surface arising from solution of a sequence of homogeneous Helmholtz PDE's. Fourth, instead of spherical harmonics we apply the faster Cheong's double Fourier series [8] to solve each of these Helmholtz PDE's. These four attributes are the essence of our fast spectral method.

This paper is organized as follows. In the next section, we briefly review the use of PDE's and variational principles as applied to surface reconstruction and 3D active contours. In Section III, the spectral method on the unit sphere proposed by Cheong is described. Simulation and experimental results are provided in Section IV; and finally in Section V, we discuss current limitations of the methods and future research directions. The reader interested in more details and additional applications of surface reconstruction. segmentation, and registration is referred to the thesis [20].

II. PDE IN SURFACE RECONSTRUCTION AND 3D ACTIVE CONTOURS

A. Surface Reconstruction

Let $g = g(\theta, \phi)$ be a noisy radial function, called the edge map, obtained from the coarse segmentation of a star-shaped object. The surface reconstruction problem is to use some form of regularization to approximate the rough edge map $g(\theta, \phi)$ by a smooth function $f(\theta, \phi)$. Variational approaches to this problem specify the

solution f as a critical point which minimizes the energy functional [11]:

$$E(f,g) = \mu \int_{S^2} Y(f,g) d\Omega_{S^2} + \int_{S^2} Z(f) d\Omega_{S^2}, \tag{2}$$

where Y measures the distance between the function f and the coarse segmentation data g, Z is a measure of reconstruction smoothness, and μ controls the tradeoff between the faithfulness to the segmentation data and smoothness of the surface. The two terms in E represent the faithfulness to the segmentation data, called the data fidelity term, and the regularization penalty, called the smoothness term, respectively. If we define the data fidelity as a metric $Y(f,g) = (f(\theta,\phi) - g(\theta,\phi))^2$, the approach becomes penalized least squares fitting which is the classic reconstruction method. The smoothing term frequently contains the derivative of the function f to enforce smoothness. For instance, Z can be defined to be $Z(f) = \|\nabla f\|^2$, where ∇ is the gradient operator. With these choices, the energy functional is completely defined,

$$E(f,g) = \int_{S^2} \mu (f(\theta,\phi) - g(\theta,\phi))^2 d\Omega_{S^2} + \int_{S^2} \|\nabla f(\theta,\phi)\|^2 d\Omega_{S^2}. \tag{3}$$

The reconstruction objective is to minimize $E(f,g)$ over f. Using the calculus of variations [13], a stationary point of the above energy functional can be found by solving the associated Euler-Lagrange equation:

$$\nabla^2 f - \mu(f - g) = 0. \tag{4}$$

When specialized to spherical coordinates this becomes a elliptic equation of Helmholtz type [1], a fact that will be used in the sequel. When a time variable is included in the energy minimization functional (3) the elliptic equation becomes a function over time and space. When indexed by the time variable the solution to (4) is called an evolving surface or active contour.

Although finite difference methods (FDM) and finite element methods (FEM) have been employed to solve the elliptic equation (4), they are iterative and thus have higher computational complexities than the spectral method that will be introduced in Section II. In Section II-B, we will show that a non-linear PDE similar to (4) can be used to reconstruct 3D star-shaped surfaces with missing or broken edges. Due to the non-linearity of this PDE, we will see that it has to be solved by the fast spectral method sequentially in time.

B. Parametric Active Contours on the Unit Sphere

Parametric active contour methods can solve image segmentation problem and surface reconstruction problem simultaneously. Let $\mathbf{x}$ be a mapping $\mathbf{x} : \Omega \to \mathbb{R}^3$, where Ω is a subset of $\mathbb{R}^2$, and represent a propagating surface in a parametric active contour approach, an energy functional E associated with $\mathbf{x}$ can be defined as:

$$E(\mathbf{x}) = \int_{\Omega} \left([\alpha \|\nabla \mathbf{x}\|^2 + \beta \|\nabla^2 \mathbf{x}\|^2] + P_{\text{ext}}(\mathbf{x}) \right) d\Omega \tag{5}$$

where α and β are parameters controlling the smoothness of $\mathbf{x}$ and P_{ext} represents a potential function. It is clear that two kinds of energy constitute the energy functional. The term $\int_{\Omega} \alpha \|\nabla \mathbf{x}\|^2 + \beta \|\nabla^2 \mathbf{x}\|^2 d\Omega$, which is computed from the contour $\mathbf{x}$ itself, is called internal energy. The term $\int_{\Omega} P_{ext}(\mathbf{x}) d\Omega$, which is computed from the image and current location of $\mathbf{x}$, is called external energy. The force generated by the internal energy disencourages the stretching and bending of the contour, in other words, has regularization effect on the contour, while the force generated by the external energy attracts the contour towards the object boundary. Therefore, the external energy represents the segmentation function of the active contour, and the internal energy represents the reconstruction function of the active contour. The contour $\mathbf{x}$ deforms under these two kinds of forces to find a minimizer of the energy functional E.

The external force field plays an important role in active contour methods. Typically, active contours are drawn towards the desired boundary by the external force which could include one or more of the following

components: a traditional potential force, obtained by computing the negative gradient of an attraction potential defined over the image domain [11], [18]; a pressure force, used by Cohen in his balloon model [11], which could be either expanding or contracting depending on whether the contour is initialized from inside or outside; or a gradient vector flow, used by Xu [33] and obtained by diffusion of edge-map's gradient. The role of the external force is such that it must contain adequate boundary information to give it sufficient capture range.

Let $I : \mathbb{R}^3 \rightarrow \mathbb{R}$ represent the grey scale image volume to be segmented, $g := \{x_g, y_g, z_g\}$ be the set of all edge points detected in I, and $d(g,(x,y,z))$ be the distance from a point (x,y,z) in the evolving surface $\mathbf{x}$ to its nearest edge point, i.e. $d(g,(x,y,z)) \triangleq \min_{(x_g,y_g,z_g)\in g} \|(x,y,z)-(x_g,y_g,z_g)\|$. Figure 1 illustrates these relations. Potential functions designed to deform the active contour usually have a global minimum at the object boundary. Two common types of potential functions are:

$$P_{(1)}(\mathbf{x}) = h_1(\nabla I(\mathbf{x})) \tag{6}$$

$$P_{(2)}(\mathbf{x}) = h_2(d(g,\mathbf{x})) \tag{7}$$

where h_1 and h_2 are functions making $P_{(1)}$ and $P_{(2)}$ convex at the location of object boundary. For instance, $P(x,y,z) = -|\nabla I(x,y,z)|^2$, $P(x,y,z) = -|\nabla G_\sigma(x,y,z) * I(x,y,z)|^2$ and $P(x,y,z) = \frac{1}{1+|\nabla I|^p}$ belong to the type of $P_{(1)}$. In fact, $|\nabla I|$ serves as an edge detector which locates sharp intensity changes in image I. Potential functions of the type $P_{(1)}$ have the disadvantage that the resulting external force has very small capture range because $P_{(1)} \approx 0$ in homogeneous intensity areas. Potential functions of type $P_{(2)}$ solve this problem by incorporating the use of edge points extracted by local edge detectors. The common choices of $P_{(2)}$ are $P(x,y,z) = d^2(g,(x,y,z))$, $P(x,y,z) = \frac{-1}{d(g,(x,y,z))}$ and $P(x,y,z) = -e^{-d^2(g,(x,y,z))}$. The boundary location has been broadcasted to many of their neighbors through the value of d. In our experiment, we chose $d^2(g,\mathbf{x})$, a $P_{(2)}$ type potential function, to generate the external force for the active contour. This external force will make the active contour evolve towards the boundary along a path of minimal distance.

In (5), $\alpha\|\nabla\mathbf{x}\|^2$ and $\beta\|\nabla^2\mathbf{x}\|^2$ control the active contour's elasticity and rigidity separately. The regularization effect coming from $\alpha\|\nabla\mathbf{x}\|^2$ can be interpreted as a curvature based flow which has very satisfactory geometric smoothing properties [19], [24]. A theorem in differential geometry states that any simple closed curve moving under its curvature collapses to a circle and then disappears. Therefore, a bigger α implies a bigger stretching force, so that the active contour resists more the stretching, tends to shrink and have an intrinsic bias toward solutions that reduce the active contour curve length or surface area. On the other hand, a bigger β implies a larger resistance to tensile stress and bending. If we set $\beta = 0$ to allow second-order discontinuity in the active contour, the equation (5) is then reduced to

$$E(\mathbf{x}) = \int_\Omega \alpha\|\nabla\mathbf{x}\|^2 + d^2(g,\mathbf{x})d\Omega \tag{8}$$

For star-shaped contours, it will be convenient to convert the surface $\mathbf{x}$ expressed in $\mathbb{R}^3$, into a radial description function $f(\theta,\phi)$ which expresses the surface in the object-centered spherical coordinate system. As we will see, this conversion not only simplifies the contour expression, but also permits speed-up of the contour evolution by application of spectral methods. When there are missing or broken edges the edge map g is not specified for all angles θ,ϕ and the data fidelity term cannot be directly implemented in (8). To deal with this we follow a similar procedure to that of Cohen *etal* [10] and use a Chamfer-like distance function to compute the data fidelity term. Specifically, we define a modified data fidelity term as

$$d(g,\mathbf{x}) = d(g,f) = \|f(\theta,\phi) - g_f(\theta,\phi)\| \tag{9}$$

where $g_f(\theta,\phi)$ is defined as the point on edge map which is closest to the point $f(\theta,\phi)$ on the evolving surface

$$g_f(\theta,\phi) \triangleq \left\| \arg\min_{(x_g,y_g,z_g)\in g} \|(x_g,y_g,z_g) - (f\sin\theta\cos\phi, f\sin\theta\sin\phi, f\cos\theta)\| - (x_o,y_o,z_o) \right\| \tag{10}$$

and (x_o, y_o, z_o) represents the coordinates of object center. The function g_f will be referred to as the closest edge map. See Figure 1 for illustration.

The equation (8) can now be rewritten as:

$$E(f) = \int_{S^2} \alpha \|\nabla f\|^2 + (f - g_f)^2 d\Omega_{S^2}. \tag{11}$$

Although equation (11) is analogous to equation (3), its associated Euler-Lagrange equation is a little different as compared to equation (4). Since g_f is a non-linear function of f, the calculus of variations leads to a more complicated Euler-Lagrange equation:

$$\alpha \nabla^2 f - f = -(f - g_f)\frac{\partial g_f}{\partial f} - g_f, \tag{12}$$

where $\partial g_f / \partial f$ is a suitably defined variational of the closest edge map as a function of the surface. While it would be worthwhile to explore conditions for existence of this variational we will sidestep this issue by making the approximation $|(f - g_f)\frac{\partial g_f}{\partial f}| \ll g_f$ in (12). This approximation can be justified in the case that the edge surface g_f encloses a large region and that f is close to g_f. To apply the fast spectral method to solve the elliptic PDE (12) has to be linearized so that it becomes a homogeneous Helmholtz-type PDE. We will describe such a manipulation in Section II-D.

C. Volumetric Penalization

Traditional parametric and geometric active contours solely rely on the local edge detector to stop the curve propagation. These methods do not use any region-based or volume-based information in the image. Such active contours can only segment and reconstruct objects whose boundaries are well defined by gradient $|\nabla I|$ of the image. For objects with blurred or even broken boundaries, traditional active contour may pass through the boundary. In [7], Chan proposed to use Mumford-Shah energy functional [22] to deal with this "boundary leakage" problem. Similar approaches to include region-based information in segmentatioin can also be found in [17] and [32]. We use the same method as in [7] to incorporate the volume information into the energy functional of 3D active contour. The volume information is introduced as an additional penalty function. Define a new energy functional $E_{\text{vol}}(f)$ associated with f as:

$$\begin{aligned} E_{\text{vol}}(f) &= \gamma \left(\int_{\text{inside}(f)} (I - u_{\text{in}})^2 dV + \int_{\text{outside}(f)} (I - u_{\text{out}})^2 dV \right) \\ &= \gamma \left(\int_{S^2} \left(\int_{r=0}^{f(\theta,\phi)} (I - u_{\text{in}})^2 r^2 dr + \int_{f(\theta,\phi)}^{B(I)} (I - u_{\text{out}})^2 r^2 dr \right) d\Omega_{S^2} \right) \end{aligned} \tag{13}$$

where $I = I(r, \theta, \phi)$ is the gray level intensity of the 3D image, $B(I)$ represents the boundary of the image I, and u_{in} and u_{out} are the mean intensities in the interior of the evolving surface f and respectively outside f

$$u_{\text{in}} = \frac{\int_{\text{inside}(f)} I dV}{\text{vol}(\text{inside}(f))}, \qquad u_{\text{out}} = \frac{\int_{\text{outside}(f)} I dV}{\text{vol}(\text{outside}(f))}. \tag{14}$$

Here the denominators in (14) are the volume inside and outside the evolving surface. With the assumption that the image intensity is near homogeneous inside and outside the object boundary, the new energy functional (13) has the same minimizer as (11), which is the contour of the object boundary. It can be adjoined to the Lagrangian (11) by aggregating the integrals over S^2:

$$\begin{aligned} E(f) &= \int_{S^2} \Big\{ \alpha \|\nabla f\|^2 + (f - g_f)^2 + \\ &\qquad \gamma \Big[\int_0^f (I - u_{\text{in}})^2 r^2 dr + \int_f^{B(I)} (I - u_{\text{out}})^2 r^2 dr \Big] \Big\} d\Omega_{S^2} \end{aligned} \tag{15}$$

Now calculus of variations can be applied to obtain the necessary condition for minimization of this volumetrically penalized Lagrangian

$$\alpha\nabla^2 f - (f - g_f)(1 - \frac{\partial g_f}{\partial f}) - \gamma z(f, I) = 0 \tag{16}$$

where

$$\begin{aligned} z(f,I) &= f^2 \cdot [(I(f) - u_{\text{in}})^2 - (I(f) - u_{\text{out}})^2] + 2(\frac{\delta u_{\text{in}}}{\delta f}) \int_0^f r^2 (I - u_{\text{in}}) dr \\ &\quad + 2(\frac{\delta u_{\text{out}}}{\delta f}) \int_f^{B(I)} r^2 (I - u_{\text{out}}) dr \end{aligned} \tag{17}$$

and

$$\frac{\delta u_{\text{in}}}{\delta f} = \frac{\int_{S^2} f^2 I(f) d\Omega_{S^2} - u_{\text{in}}\ \text{surf}(f)}{\text{vol}(\text{inside}(f))} \tag{18}$$

$$\frac{\delta u_{\text{out}}}{\delta f} = -\frac{\int_{S^2} f^2 I(f) d\Omega_{S^2} - u_{\text{out}}\ \text{surf}(f)}{\text{vol}(\text{outside}(f))} \tag{19}$$

where $\text{surf}(f) = \int_{S^2} f^2 d\Omega_{S^2}$ is the surface area of the evolving contour.

D. Evolution Algorithm

Comparing equation (16) with (4), it is clear the Euler-Lagrange equation (16) is no longer a homogeneous Helmholtz PDE. First, the functional dependence of g_f on f makes the equation non-linear in f. Second, the additive volumetric penalization term z is not linear in f and is not "instantaneous" in (θ, ϕ). The same issue was encountered in [17] and the authors got around it by linearization of in f about the contour computed in the previous step followed by update propagation. Update propagation is a kind of successive approximation scheme for which, iteration $n + 1$, we update f_n in terms of past iterate $f_n(\theta', \phi')$, if f_{n+1} for (θ', ϕ') has not yet been computed, and a partial update $f_{n+1}(\theta', \phi')$ if f_{n+1} for (θ', ϕ') has been computed. This succesive approximation idea can be similarly applied to linearize our equation (16) so that it takes the form of a homogeneous linear Helmholtz equation. Combining all the non-linear terms in the PDE into a single term and moving it to the right side of the equation, (16) is rewritten as:

$$\alpha\nabla^2 f - f = \gamma z(f, I) - (f - g_f)\frac{\partial g_f}{\partial f} - g_f. \tag{20}$$

Invoking the assumed dominance condition $|(f - g_f)\frac{\partial g_f}{\partial f})| \ll g_f$, and replacing the right hand side of (20) with with the value of f_n we obtain a linearized homogeneous Hemholtz equation

$$\alpha\nabla^2 f_{n+1} - f_{n+1} = \gamma z(f_n, I) - (f_n - g_{f_n}) - g_{f_n}. \tag{21}$$

This evolution is different from contour evolution in FDM, which could be implemented by the iteration

$$f_{t+\Delta t} = f_t + [\alpha\nabla^2 f_t - (f_t - g_{f_t})(1 - -\gamma z(f_t, I)]\Delta t \tag{22}$$

where Δt is the FDM time step which indexes the evolving surfaces.

The details of the evolution algorithm is as following:

1. Initialize the evolution with $f_0 = c$, c is determined by the object size;
2. Compute $g_{f_n}(\theta, \phi)$ and update the RHS of (21) with f_n and g_{f_n};

3. Solve PDE $\alpha\nabla^2 f_{n+1} - f_{n+1} = \gamma z(f_n, I) - (f_n - g_{f_n})\frac{\partial g_{f_n}}{\partial f_n} - g_{f_n}$ with spectral method to get the new contour f_{n+1};

4. Compute the error, $e_{n+1} = \sqrt{\frac{\sum_{i=0}^{M-1}\sum_{j=0}^{N-1}(f_n(\theta_i,\phi_j)-f_{n+1}(\theta_i,\phi_j)^2}{MN}}$

5. if $e_n >$ threshold, go back to 2,

else end.

In the above algorithm, α and γ are chosen in advance to control the tradeoff between surface fidelity to the edge map and surface smoothness.

III. 3D Spectral Approach

As we have discussed in the introduction, FDM [33] and FEM [11] have been used to solve the Euler-Lagrange equations associated with the surface reconstruction and active contours. However, all of these methods have difficulties in 3D images due to the large grid size necessary for 3D images. Spectral methods for solving PDE's over a 2D rectangular domain are well known for their faster rate of convergence and higher accuracy as compared to iterative FEM and FDM. These methods usually take advantage of symmetries by transforming the equation into spectral domain and only require $O(N^2 \log N)$ operations for a 2D problem on $N \times N$ grid. It was Simchony who first applied spectral method to solve Poisson equations on 2D rectangles in computer vision problems [26]. Although similar methods for solving PDE's over the unit sphere have been used in numerical weather prediction and the study of ocean dynamics [8], [34], to the best of our knowledge, they have not been used in 3D computer vision problems.

Since our problem is in spherical geometry, basis functions, such as spherical harmonics, double Fourier series and Chebyshev polynomials, all have attractive features. A good comparison of these functions is given by Boyd in [3]. Due to the spherical geometry, some conditions must be imposed on the basis functions to ensure that the approximated radial function and its corresponding derivative are continuous at poles. For the details of pole problem, readers are refered to [4]. The spherical harmonics are best with regard to the pole problems because of the property of the associated Legendre functions, but the Legendre functions also make the computation of spherical harmonics the most complex among the three basis sets. On the other hand, double Fourier series can give comparable accuracy and are significantly easier to program. Most of all, the existing FFT makes double Fourier series the most efficient transform method.

Yee first applied truncated double Fourier series to solve Poisson-type equations on a sphere [34]. However, Yee's algorithm had the deficiency of not properly enforcing continuity at the spherical poles, the so called pole conditions. Recently, Cheong proposed a new method which is similar to Yee's method, but directly enforces the pole conditions and leads to increased accuracy and stability for time-stepping PDE solution procedures [8]. In the subsequent sections, we discuss the application of Cheong's spectral method to solve the Helmholtz equations associated with the surface reconstruction problem and evolving 3D active contours. Notice that μ in the equation $\nabla^2 f - \mu(f - g) = 0$ and α in the equation $\alpha\nabla^2 f - (f - g_f)(1 - \frac{\partial g_f}{\partial f}) = 0$ are both regularization parameters. We can unify the two notations by setting $\alpha = 1/\mu$ so that after the linearization, the PDE $\alpha\nabla^2 f - (f - g_f)(1 - \frac{\partial g_f}{\partial f}) = 0$ also takes the simple homoegenous Helmholtz form $\nabla^2 f - \mu(f - g) = 0$.

A. The Spectral Method

We describe the spectral method proposed by Cheong in this section. The elliptic equation $\nabla^2 f - \mu(f - g) = 0$ is a Helmholtz equation. The Laplacian operator ∇^2 on the unit sphere is of form:

$$\nabla^2 = \frac{1}{\sin\theta}\frac{\partial}{\partial\theta}(\sin\theta\frac{\partial}{\partial\theta}) + \frac{1}{\sin^2\theta}\frac{\partial^2}{\partial^2\phi}. \tag{23}$$

We assume the value of function f and g are given on the grid (θ_j, ϕ_k), $\theta_j = \pi(j + 0.5)/J$ and $\phi_k = 2\pi k/K$, where J and K are the number of data points along the latitude and longitude, separately. We can expand the

function g, and similarly for f, with a Fourier series in longitude with a truncation M, e.g.,

$$g(\theta,\phi)=\sum_{m=-M}^{M} g_m(\theta)e^{im\phi_k} \tag{24}$$

where $g_m(\theta)$ is the complex Fourier coefficient given by $g_m(\theta)=\frac{1}{K}\sum_{k=0}^{K-1} g(\theta,\phi_k)e^{-im\phi_k}$, $\phi_k=2\pi k/K$ and $K=2M$. The equation (4) can then be written as an ordinary differential equation:

$$\frac{1}{\sin\theta}\frac{d}{d\theta}\left(\sin\theta\frac{d}{d\theta}f_m(\theta)\right)-\frac{m^2}{\sin^2\theta}f_m(\theta)=\mu[f_m(\theta)-g_m(\theta)] \tag{25}$$

The latitude function $f_m(\theta)$ and $g_m(\theta)$ can be further approximated by the truncated sine or cosine functions,

$$\begin{aligned} g_m(\theta_j) &= \sum_{n=0}^{J-1} g_{n,0}\cos n\theta_j, && m=0 \\ g_m(\theta_j) &= \sum_{n=1}^{J} g_{n,m}\sin n\theta_j, && \text{odd } m \\ g_m(\theta_j) &= \sum_{n=1}^{J} g_{n,m}\sin\theta_j\sin n\theta_j, && \text{even } m\neq 0. \end{aligned} \tag{26}$$

This is Cheong's method and an efficient procedure for calculating the spectral coefficients $g_{n,m}$ can be found in [8]. After substitution of (27) into (25), we get an algebraic system of equations in Fourier space:

$$\begin{aligned} \frac{(n-1)(n-2)+\mu}{4}f_{n-2,m}-\frac{n^2+2m^2+\mu}{2}f_{n,m}+\frac{(n+1)(n+2)+\mu}{4}f_{n+2,m} \\ =\mu[\frac{1}{4}g_{n-2,m}-\frac{1}{2}g_{n,m}+\frac{1}{4}g_{n+2,m}],\ m=0,\text{ or odd} \end{aligned} \tag{27}$$

and

$$\begin{aligned} \frac{n(n-1)+\mu}{4}f_{n-2,m}-\frac{n^2+2m^2+\mu}{2}f_{n,m}+\frac{n(n+1)+\mu}{4}f_{n+2,m} \\ =\mu[\frac{1}{4}g_{n-2,m}-\frac{1}{2}g_{n,m}+\frac{1}{4}g_{n+2,m}],\ m\text{ even}\neq 0 \end{aligned} \tag{28}$$

where $n=1,3,\cdots,J-1$ for odd n, $n=2,4,\cdots,J$ for even n if $m\neq 0$ and $n=0,2,\cdots,J-2$ for even n, $n=1,3,\cdots,J-1$ for odd n if $m=0$. This says the components of even and odd n are uncoupled for a given m. The equations (27) and (28) can be rewritten in matrix format,

$$B\mathbf{f}=\mathbf{A}\mathbf{g} \tag{29}$$

where B and A are matrices of size $J/2\times J/2$ with tridiagonal components only, $\mathbf{f}$ and $\mathbf{g}$ are column vectors whose components are the expansion coefficients of $f_m(\theta)$ and $g_m(\theta)$. For example, the subsystem for odd n looks like this:

$$\begin{pmatrix} b_{1,m} & c_1 & & & \\ a_3 & b_{3,m} & c_3 & & \\ & \ddots & \ddots & \ddots & \\ & & a_{J-3} & b_{J-3,m} & c_{J-3} \\ & & & a_{J-1} & b_{J-1,m} \end{pmatrix}\begin{pmatrix} f_{1,m} \\ f_{3,m} \\ \vdots \\ f_{J-3,m} \\ f_{J-1,m} \end{pmatrix}=$$

$$\begin{pmatrix} 2 & -1 & & & \\ -1 & 2 & -1 & & \\ & \ddots & \ddots & \ddots & \\ & & -1 & 2 & -1 \\ & & & -1 & 2 \end{pmatrix}\begin{pmatrix} g_{1,m} \\ g_{3,m} \\ \vdots \\ g_{J-3,m} \\ g_{J-1,m} \end{pmatrix}$$

The procedure to solve the equation (4) is as follows: First, we get $g_{n,m}$, the spectral components of $g(\theta, \phi)$ by double Fourier series expansion. Then the right hand side of (29) is calculated to obtain the column vector $\mathbf{g_1} = \mathbf{Ag}$. Finally, the tridiagonal matrix equation $B\mathbf{f} = \mathbf{g_1}$ is solved and $f(\theta, \phi)$ is obtained by inverse transform of $f_{n,m}$. Notice that the Poisson equation $\nabla^2 f = g$ is just a special case of Helmholtz equation, so that a slight modification in the above algorithm will give the solution to homogeneous Poisson equations. Other homogeneous elliptic equations, such as biharmonic equations can also be solved by this spectral method.

B. Complexity Analysis

Consider an elliptic equation with a grid size of $N \times N$ on unit sphere. If FEM were used, there would be a total of N^2 variables with matrix size $N^2 \times N^2$. A crude Gauss elimination method will require $O(N^6)$ operations and the Gauss-Siedel relaxation will require $O(N^4)$ operations to converge. The number of operations might be reduced to $O(N^3)$, if the algorithms can use the fact that the matrix is sparse,. However the computational complexity of the spectral method described above is only $O(N^2 \log N)$ (see [8]). The complexity of the spectral method on the unit sphere is in the same order as that of FEM applied on a grid over a rectangle. We are writing the program for the detailed running time comparison of the FEM and the spectral method applied in the active contour segmentation. In [25], Shen performed a numerical experiment which applied two spectral methods and the FDM to solve the same Helmholtz equation on the sphere. The CPU time comparison in [25] indicates that the spectral method based on double Fourier expansion is significantly more efficient and/or accurate when compared with the algorithm based on spherical harmonics and on finite difference. The experiments in [21] showed the similar results.

IV. Applications

Here we illustrate the spectral method for simulated and real 3D image volumes.

A. Surface Reconstruction

For the surface reconstruction problem the algorithm was applied to synthesized segmentation data to show the effect of different choices of regularization parameter μ for different noise levels and for different shapes. The object center is assumed to be known or to have been estimated in advance.

We first performed experiments to compare reconstructions of a sphere and an ellipsoid in order to illustrate the role of the regularization parameter α. Simulated the effect of isotropic segmentation noise by adding circular Gaussian segmentation noise to the spherical harmonic coefficients. In Figure 2, the reconstruction error is plotted versus the value of $\mu = 1/\alpha$ for two shapes. The straight line represents the standard deviation of the segmentation noise. The figure shows that for the simple spherical shape, which only contains a single frequency component, the value of μ should be as small as possible in order to filter out segmentation noise, while for a shape containing higher spatial frequencies, such as the ellipsoid, μ should be optimized to control the tradeoff between denoising and matching high spatial frequencies. Note that as the standard norm of the gradient is adopted to enforce smoothness, a spherical surface minimizes the energy function for $\mu = 0$. When the edge map is derived from an ellipsoidal surface the optimum value of μ lies between 10^1 and 10^2. If μ is too small the evolving surface is overly attracted to the mismatched spherical shape while if μ is too high, the segmentation noise dominates te reconstruction. One possible method for improvement is to use prior information to induce more suitable shape attractors by implementing a weighted norm on the evolving surface gradient.

The optimum value of μ not only changes with different shapes, but also with different noise levels. In a second experiment, the choice of μ for different segmentation noise levels was investigated. Different levels of Gaussian noise are added to the ellipsoidal shape. Figure 3 shows that μ should be smaller for low SNR segmentation data than for high SNR segmentation data, which is as expected. Three reconstructions of the ellipsoid are presented in Figure 4. As previously described, the goodness of fit of the final reconstructed surfaces is determined by the value of μ.

B. 3D Parametric Active Contours

B.1 Active Contour with Volumetric Penalization

The volumetric penalization method described in Secs. II and III was applied to a synthesized 3D image to show the effect of leakage prevention. An ellipsoid is contained in a $128 \times 128 \times 64$ image. One side of the ellipsoid boundary has been blurred with a linear filter, a single slice of which is shown in Figure 8. The set of edgemaps of the blurred 3D image is shown in Figure 9 and were derived from the blurred image by the Canny edge detector implemented in the MATLAB function edge(). Both the blurred grey-level image and the set of extracted edgemaps were then used to drive our volumetrically penalized active contour algorithm . Figure 10(a) shows that without volumetric penalty leakage of the contour occurs in the vicinity of the blurred boundary. Figure 10(b) illustrates the positive effect of volumetric penalization. In this experiment, we chose $\alpha = 10^6$ and $\gamma = 5\alpha$. The penalization in each direction is proportional to f^2. How to automatically choose the parameters α and γ is a topic worthy of additional study.

B.2 Liver Shape Extraction

In this experiment, we applied the active contour algorithm (without volumetric penalty) to 3D human liver extraction from an actual thoracic X-ray CT scan. The X-ray CT image was obtained as a stack of 2-D image slices each of size 256×256. Double Fourier series were used to expand the radial function of a 3D sphere initialized inside the liver volume. The edge maps were again obtained by Canny filtering. The CT slices and the corresponding edgemaps are shown in Figure 5.

As in the elliposidal surface reconstruction experiment, the center of the liver was estimated in advance. Although it was not implemented in our experiment, dynamic center estimation could in principle be applied as the surface evolves. The contour was initialized as a sphere inside the liver. The initial radius was set to half of the distance from the origin to the edge point closest to it. A 32×32 grid was used for the 3D active contour. In nth iteration, the closest edge map g_{f_n} is determined from f_n and g. The elliptic equation is then solved to propagate the active contour to the new position f_{n+1}. Because the boundary information extracted by local edge detector has been integrated into the PDE, the average distance from the evolving contour to its convergent limit is within one pixel after only 5 iterations.

Figure 6 shows a slice of the final 3D surface with different values of $\alpha = 1/\mu$. When $\alpha = 10^{-3}$, the contour is over regularized and overly attracted to a spherical surface by the isotropic smoothness penalty. When $\alpha = 10^{-6}$, the regularization effect is so weak that the final contour is virtually unregularized. Empirically, it appears that $\alpha = 10^{-4}$ yields the closest match to the true outline of the liver. This further emphasizes the importance of studying the effect of the regularization parameter α. Finally, Fig. 7(a) shows the under regularized final active surface while (b) shows the final surface with $\alpha = 10^{-4}$.

V. CONCLUSIONS

In this paper, we have discussed the formulation of 3D surface reconstruction using spectral active contours with edge penalties in spherical geometry. The spectral method uses double Fourier series as orthogonal basis to solve a sequence of elliptic PDE's over the unit sphere. Compared to the complexity of $O(N^3)$ for iterative time domain (FDM) balloon methods, the complexity of $O(N^2 \log N)$ for spectral methods is significantly lower. Our experiments demonstrated fast convergence of edge penalized spectral active contours for simulated edge maps and those derived from actual 3D thoracic CT scans. We extended the 3D spectral active contour methods to volumetric penalty functions allowing the contour to account for grey-scale variations and control leakage at blurred boundaries. The choice of active contour regularization parameters requires further study. A limitation of the spectral method is that it requires a regular sampling grid and thus cannot incorporate local mesh refinement in the region of large curvatures. Another limitation is the requirement of star-shaped objects. We believe a hybrid spectral/finite-element method that provides the advantages of each should be explored to alleviate these difficulties.

REFERENCES

[1] L. Bers, F. John, and M. Schechiter, *Partial Differential Equations*, John Wiley and Sons, 1964.

[2] G. J. Boer and L. Steinberg, "Fourier series on sphere," *Atmosphere*, vol. 13, pp. 180, 1975.

[3] J. P. Boyd, "The choice of spectral functions on a sphere for boundary and eigenvalue problems: A comparison of Chebyshev, Fourier and associated Legendre expansions," *Monthly Weather Review*, vol. 106, pp. 1184–1191, Aug. 1978.

[4] J. P. Boyd, *Chebyshev and Fourier Spectral Methods*, Springer-Verlag, New York, 1989.

[5] C. Brechbühler, G. Gerig, and O. Kübler, "Parametrization of closed surfaces for 3-D shape description," *Computer Vision and Image Understanding*, vol. 61, no. 2, pp. 154–170, March 1995.

[6] V. Caselles and J. Morel, "Introduction to the special issue on partial differential equations and geometry-driven diffusion in image processing and analysis," *IEEE Transactions on Image Processing*, vol. 7, no. 3, pp. 269 –273, 1998.

[7] T. F. Chan and L. A. Vese, "Active contours without edges," *IEEE Trans. on Image Processing*, vol. 10, no. 2, pp. 266–277, Feb. 2001.

[8] H. Cheong, "Double Fourier series on a sphere: Applications to elliptic and vorticity equations," *Journal of Computational Physics*, vol. 157, no. 1, pp. 327–349, January 2000.

[9] L. D. Cohen, "On active contour models and balloons," *Computer Vision, Graphics, and Image Processing: Image Understanding*, vol. 53, no. 2, pp. 211–218, 1991.

[10] L. D. Cohen and I. Cohen, "A finite-element method applied to new active contour models and 3-d reconstruction from cross sections," in *Proc. 3rd Int. Conf Computer Vision*, pp. 587–591, 1990.

[11] L. D. Cohen and I. Cohen, "Finite-element methods for active contour models and balloons for 2-D and 3-D images," *IEEE Transactions on Pattern Analysis and Machine Intelligence*, vol. 15, no. 11, pp. 1131–1147, 1993.

[12] L. D. Cohen, "Avoiding local minima for deformable curves in image analysis," in *Curves and Surfaces with Applications in CAGD*, C. R. A. Le Méhauté and L. L. S. (eds.), editors, pp. 77–84, 1997.

[13] R. Courant and D. Hilbert, *Methods of Mathematical Physics*, Interscience, 1953.

[14] D. Gottlieb and S. A. Orszag, *Numerical Analysis of Spectral Methods: Theory and Applications*, Society for Industrial and Applied Mathematics, Philadelphia, 1977.

[15] P. Haigron, G. Lefaix, X. Riot, and R. Collorec, "Application of spherical harmonics to the modelling of anatomical shapes," *Journal of Computing and Information Technology*, vol. 6, no. 4, pp. 449–461, December 1998.

[16] B. Horn and M. Brooks, *Shape From Shading*, MIT Press, Cambridge, MA, 1989.

[17] S. Jehan-Besson, M. Barlaud, and G. Aubert, "Video object segmentation using Eulerian region-based active contours," in *Proceedings Eighth IEEE International Conference on Computer Vision*, volume 1, pp. 353–60, Vancouver, BC, Canada, July 2001.

[18] M. Kass, A. Witkin, and D. Terzopoulos, "Snakes: Active contour models," *International Journal of Computer Vision*, vol. 1, no. 4, pp. 321–331, 1987.

[19] B. B. Kimia, A. R. Tannenbaum, and S. W. Zucker, "Shapes, shocks, and deformations I: The components of two-dimensional shape and the reaction-diffusion space," *International Journal of Computer Vision*, vol. 15, no. 3, pp. 189–224, 1995.

[20] J. Li, *3D shape modeling: registration, segmentation, and reconstruction*, PhD thesis, Dept of EECS, Univ. of Michigan, Ann Arbor MI 48109-2122, January 2002.

[21] D. W. Merrill, *Finite difference and pseudospectral methods applied to the shallow water equations in spherical coordinates*, Master's thesis, The University of Colorado, 1997.

[22] D. Mumford and J. Shah, "Optimal approximation by piecewise smooth functions and associated variational problems," *Communications on pure and applied mathematics*, vol. 42, pp. 577–685, 1989.

[23] S. A. Orszag, "Fourier series on spheres," *Monthly Weather Review*, vol. 102, pp. 56–75, 1974.

[24] S. J. Osher and J. A. Sethian, "Fronts propagation with curvature dependent speed: Algorithms based on Hamilton-Jacobi formulations," *Journal of Computational Physics*, vol. 79, pp. 12–49, 1988.

[25] J. Shen, "Efficient spectral-galerkin methods iv. spherical geometries," *SIAM Journal on Scientific Computing*, vol. 20, no. 4, pp. 1438–1455, 1999.

[26] T. Simchony, R. Chellappa, and M. Shao, "Direct analytical methods for solving Poisson equations in computer vision problems," *IEEE Transactions on Pattern Analysis and Machine Intelligence*, vol. 12, no. 5, pp. 435–446, May 1990.

[27] L. H. Staib and J. S. Duncan, "Deformable fourier models for surface finding in 3d images," in *Proceedings of Vision in Biomedical Computing (VBC)*, pp. 90–94, 1992.

[28] L. H. Staib and J. S. Duncan, "Model-based deformable surface finding for medical images," *IEEE Transactions on Pattern Analysis and Machine Intelligence*, vol. 15, no. 5, pp. 1996, Oct. 1996.

[29] G. Székeley, A. Kelemen, C. Brechbühler, and G. Gerig, "Segmentation of 2-d and 3-d objects from mri volume data using constrained elastic deformations of flexible fourier contour and surface models," *Medical Image Analysis*, vol. 1, no. 1, pp. 19–34, 1996.

[30] X. Tao, J. L. Prince, and D. Christos, "Using a statistical shape model to extract sulcal curves on the outer cortex of the human brain," *IEEE Transactions on Medical Imaging*, vol. 21, no. 5, pp. 513–524, 2002.

[31] D. Terzopoulos, "Image analysis using multigrid relaxation methods," *IEEE Transactions on Pattern Analysis and Machine Intelligence*, vol. 8, pp. 129–139, March 1986.

[32] S. R. Titus, *Improved Penalized Likelihood Reconstruction of Anatomically Correlated Emission Computed Tomography Data*, PhD thesis, The Univ. of Michigan, Ann Arbor, Dec. 1996.

[33] C. Xu and J. L. Prince, "Snakes, shapes, and gradient vector flow," *IEEE Trans. on Image Processing*, vol. 7, no. 3, pp. 359–369, March 1998.

[34] S. Y. K. Yee, "Solution of Poisson's equation on a sphere by truncated double Fourier series," *Monthly Weather Review*, vol. 109, pp. 501–505, 1981.

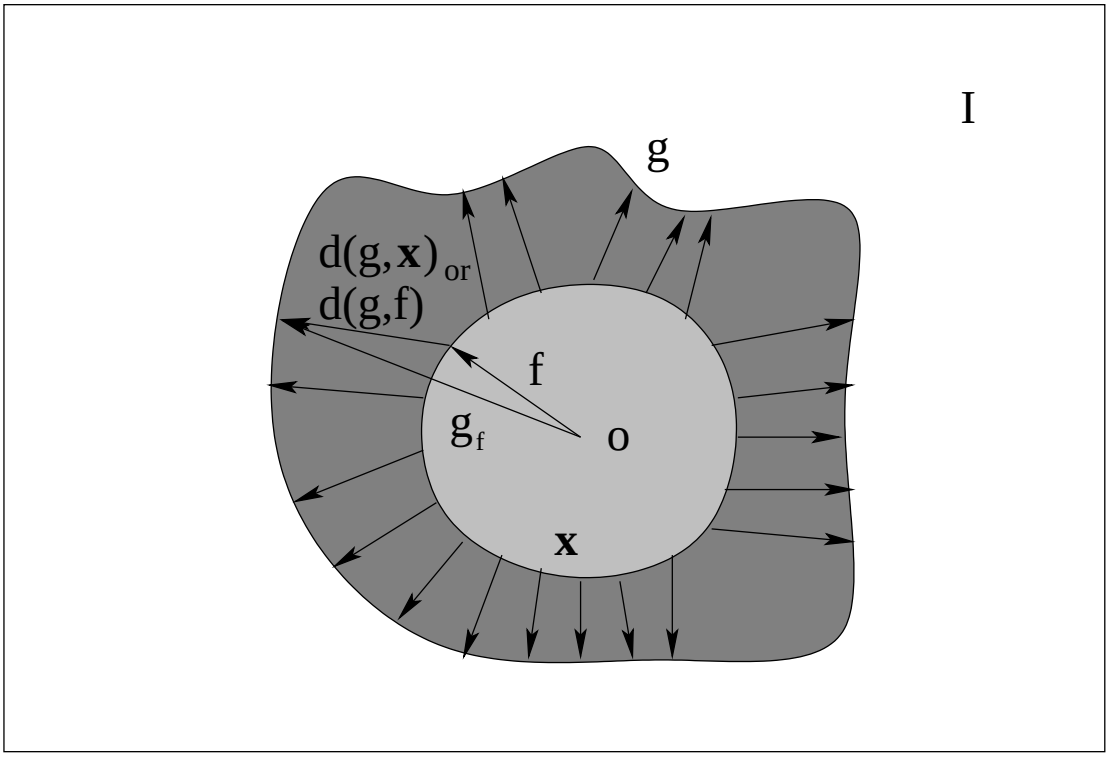

Fig. 1. A grey level image I, the set of edge points g detected in I, a propagating contour f, and $d(g, \mathbf{x})$ or $d(g, f)$, the distance between the propagating contour and its nearest edge point.

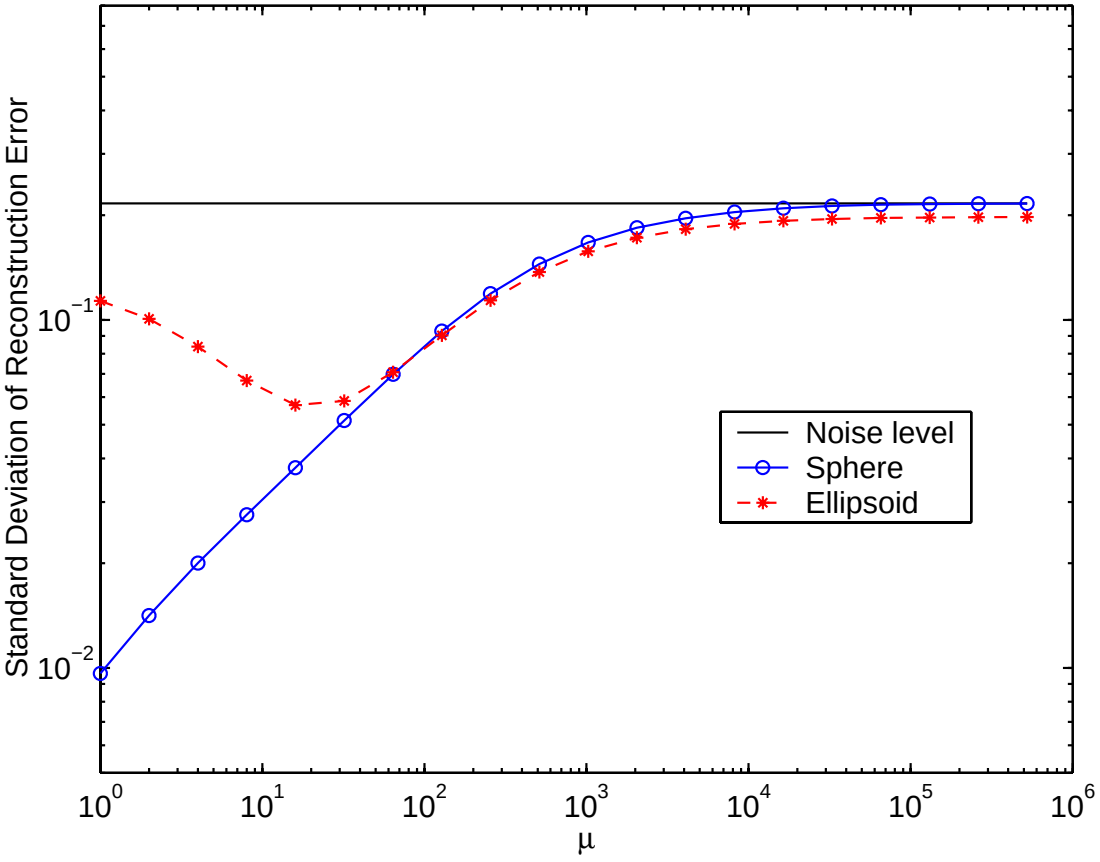

Fig. 2. Standard deviation of reconstruction error vs. $\mu = 1/\alpha$ for different shapes

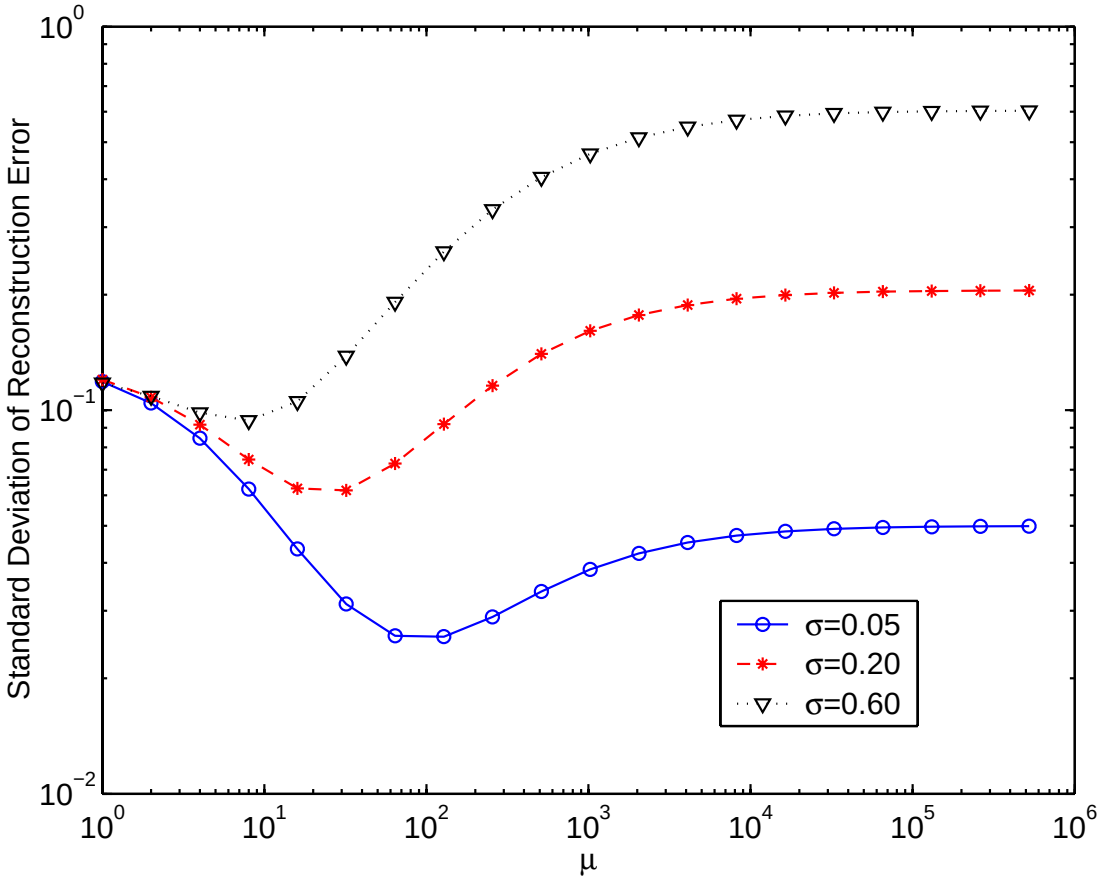

Fig. 3. Standard deviation of reconstruction error vs. $\mu = 1/\alpha$ for different segmentation noise levels

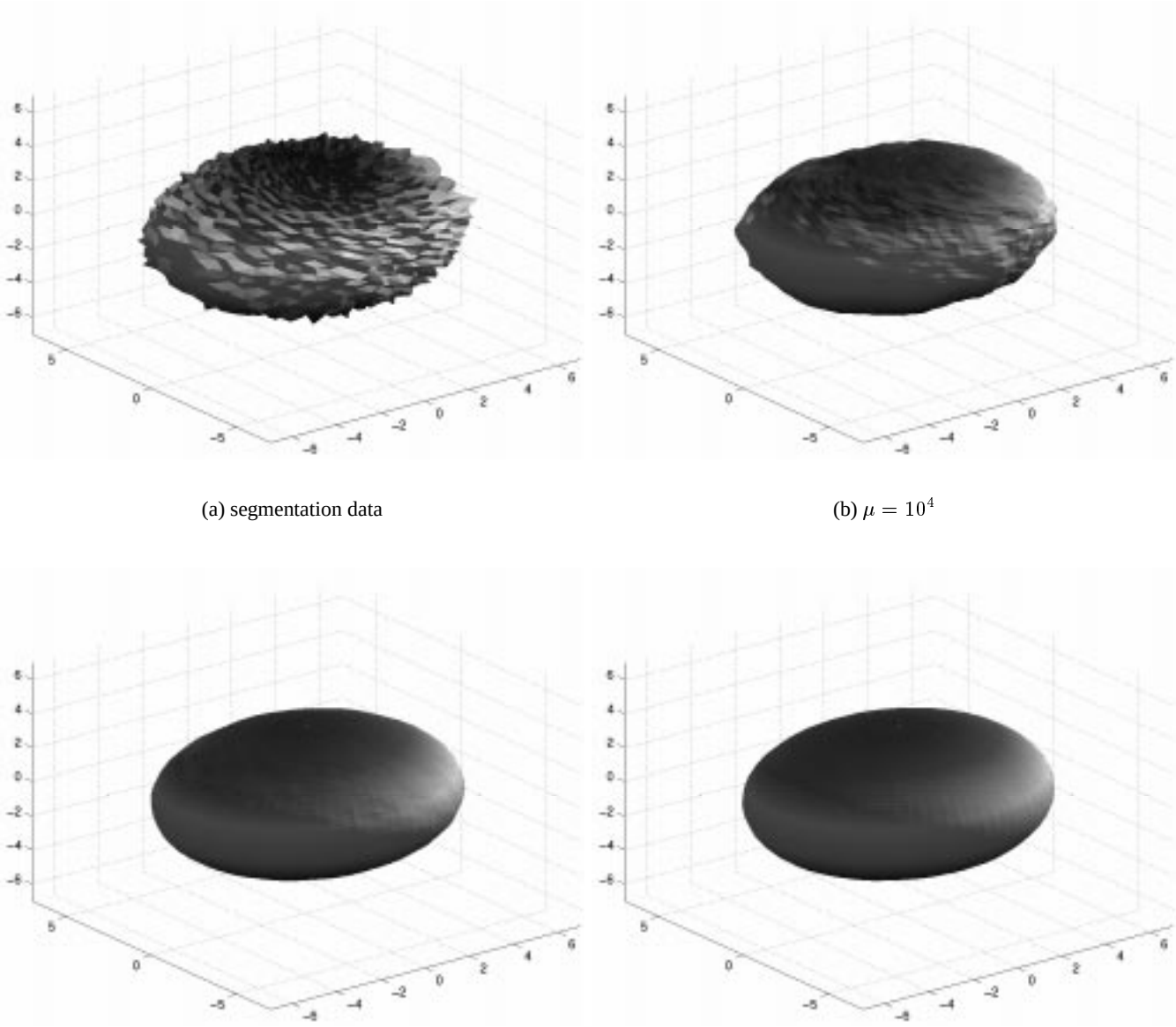

(a) segmentation data

(b) $\mu = 10^4$

(c) $\mu = 10^3$

(d) $\mu = 10^2$

Fig. 4. Final reconstruction of an ellipsoid for different values of $\mu = 1/\alpha$.

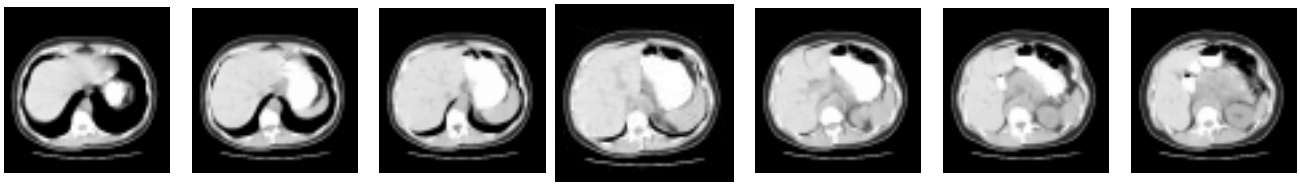

(a) (b) (c) (d) (e) (f) (g)

(h) (i) (j) (k) (l) (m) (n)

Fig. 5. CT slices and the corresponding edge maps

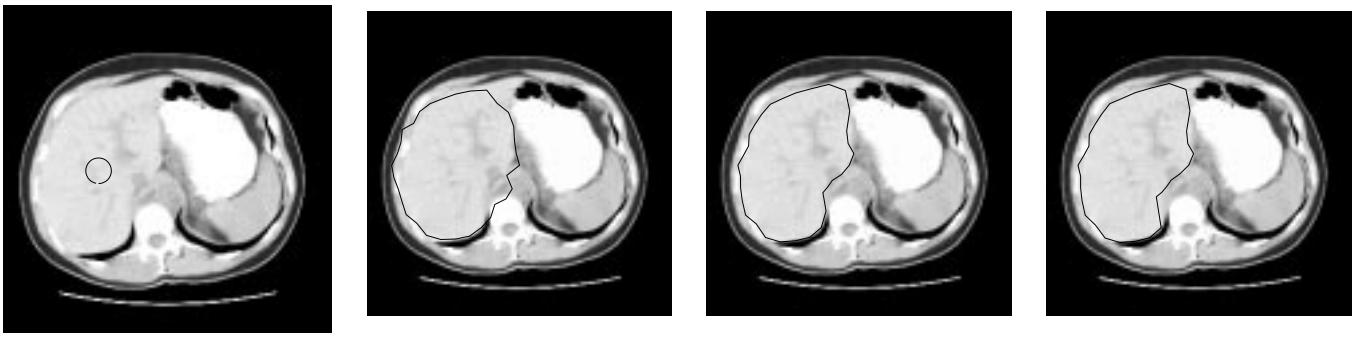

(a) Initialization (b) $\alpha = 10^{-3}$ (c) $\alpha = 10^{-4}$ (d) $\alpha = 10^{-6}$

Fig. 6. Contours solved with different α converge at different positions.

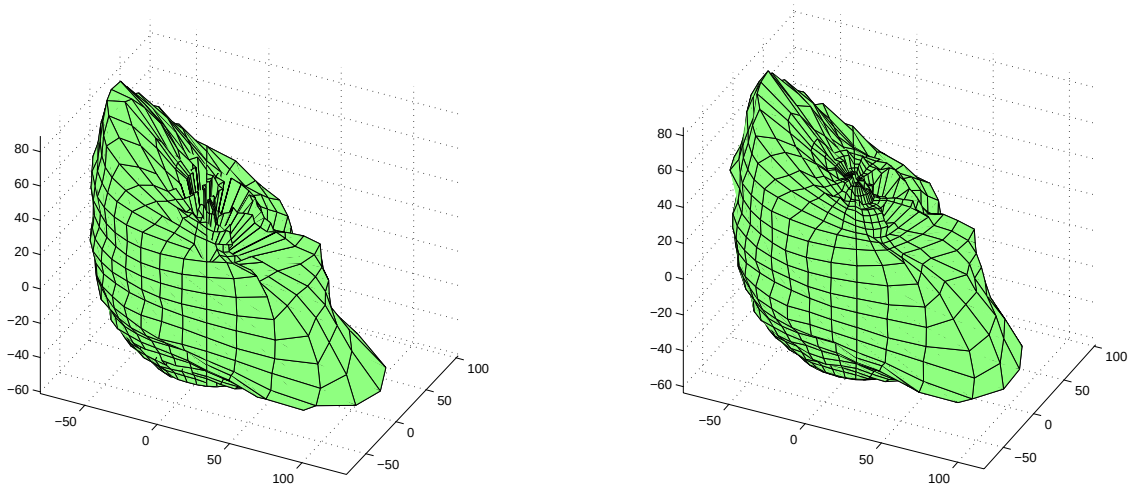

(a) Local edge detector (b) $\alpha = 10^{-4}$

Fig. 7. Comparison of shape extraction results. (a) Local edge detector; (b) Active contour.

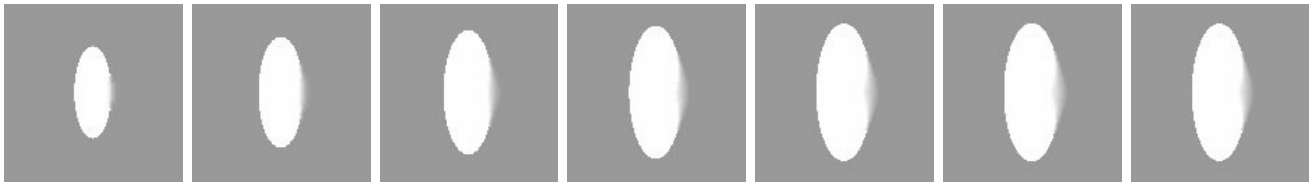

(a) (b) (c) (d) (e) (f) (g)

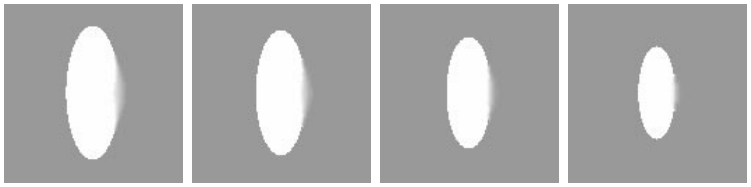

(h) (i) (j) (k)

Fig. 8. Edge-blurred Ellipsoid

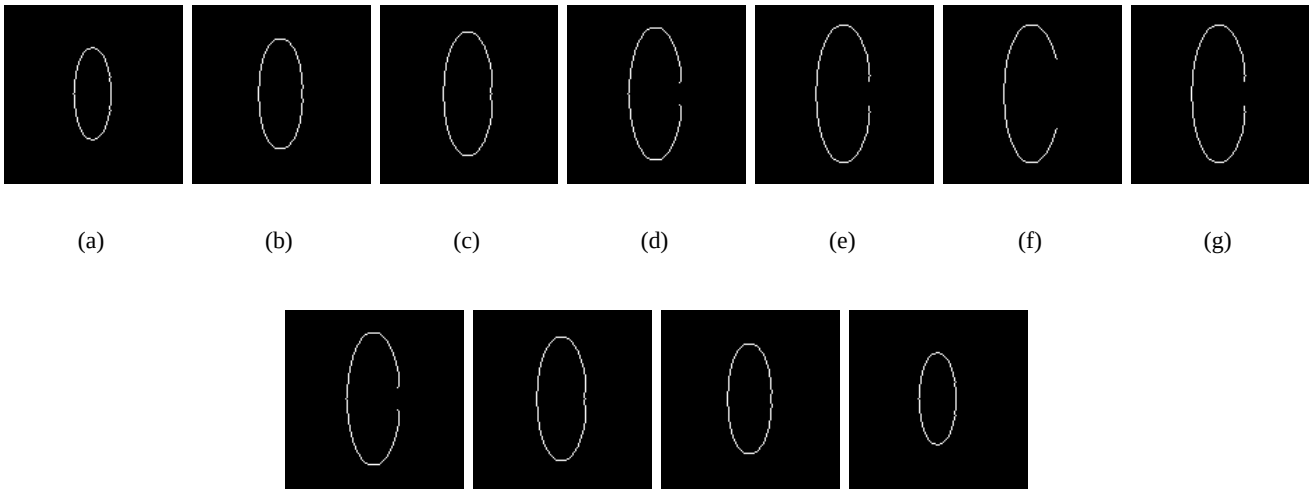

(a) (b) (c) (d) (e) (f) (g)

(h) (i) (j) (k)

Fig. 9. Edgemap of the blurred 3D image containing an ellipsoid

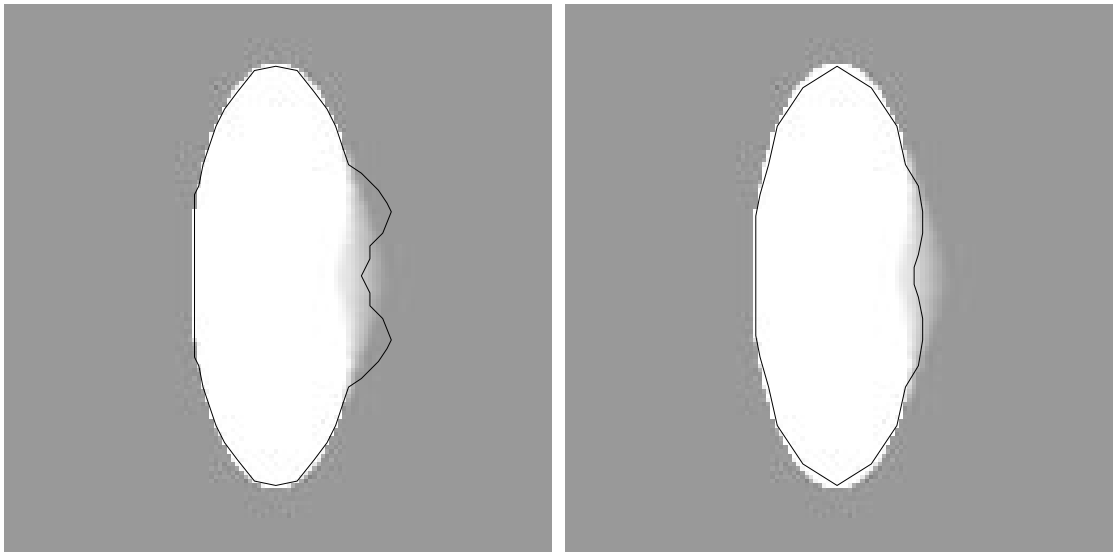

(a) No Volumetric Penalization (b) With Volumetric Penalization

Fig. 10. Segmentation results comparison between the active contours with and without volumetric penalization for edge blurred image